ADVANCED OPTICAL MATERIALS
www.advopticalmat.de

Nanoscale Surface Photovoltage Spectroscopy

*Yenal Yalcinkaya, Pascal N. Rohrbeck, Emilia R. Schütz, Azhar Fakharuddin, Lukas Schmidt-Mende, and Stefan A.L. Weber**

Understanding electron and ion dynamics is an important task for improving modern energy materials, such as photovoltaic perovskites. These materials usually have delicate nano- and microstructures that influence the device parameters. To resolve detailed structure–function relationships on the relevant micro- and nanometer length scales, the current macroscopic and microscopic measurement techniques are often not sufficient. Here, nanoscale surface photovoltage spectroscopy (nano-SPV) and nanoscale ideality factor mapping (nano-IFM) via time-resolved Kelvin probe force microscopy are introduced. These methods can map nanoscale variations in charge carrier recombination, ion migration, and defects. To show the potential of nano-SPV and nano-IFM, these methods are applied to perovskite samples with different morphologies. The results clearly show an improved uniformity of the SPV and SPV decay distribution within the perovskite films upon passivation and increasing the grain size. Nevertheless, nano-SPV and nano-IFM can still detect local variations in the defect density on these optimized samples, guiding the way for further optimization.

1. Introduction

Lead halide perovskites are promising materials for optoelectronic applications due to their direct adjustable band gap,[1–3] high defect tolerance,[4] and long charge carrier lifetimes.[5–7] Unlike conventional semiconductors, lead halide perovskites do not possess a high density of deep trap states.[8] The trap states due to crystal defects within the halide perovskites appear within or close to the energy bands. This defect tolerance allows high-quality perovskite films to be fabricated from simple solution processes. Nonetheless, energy losses still occur at areas with high defect density, such as grain boundaries (GB) of the halide perovskites or interfaces within perovskite solar cells (PSCs), increasing non-radiative recombination losses during device operations.[9]

Defects related to non-radiative recombination in perovskites mainly occur as 1D point defects such as interstitials, antisites, or vacancies; 2D defects such as GBs, interfaces, and surfaces; and 3D defects such as clusters of iodine or lead or defects at the contacts. Interfacial recombination may originate from energy alignment mismatch between layers, surface defects, and charge carrier back transfer.[10–14] Improving the perovskite film quality by means of passivation is a common strategy to improve device efficiency.[15,16] Common surface passivation methods use chemical agents that partially fill the vacancies on the perovskite film surface. Here, the active group (ammonium, for example) fills the A^+ cation vacancies, whereas other parts of the passivation agent can be used, for example, for increasing the hydrophobicity of the perovskite surface. A good example is phenylethylammonium ion (PEA^+), which contains an ammonium and a hydrophobic phenyl group.[15]

The main goal of defect passivation is to increase the efficiency of PSCs. The most common and straightforward way to characterize the perovskite film quality is therefore to measure the efficiency of PSC devices. To understand the mechanisms behind efficiency losses, however, it is helpful to characterize the perovskite layer itself. Commonly used methods aim at monitoring the charge carrier dynamics such as photoluminescence (PL)[17]; transient absorption[18]; Terahertz, microwave, or electrical impedance spectroscopy[19,20]; surface photovoltage (SPV)[21]; and surface photocurrent[22] measurements. These methods are usually conducted on macroscopic length scales and therefore yield measurements that are averaged over many different grains, GBs, and other interfaces. Local measurements such as PL microscopy[23] and fluorescence lifetime microscopy (FLIM)[24] can record and map the charge carrier dynamics. However, the lateral resolution of these optical methods is diffraction-limited and cannot fully resolve effects at the GBs. Alternatively, qualitative SPV mapping can be performed via scanning electron microscopy (SEM). Here, the electric fields generated by the local photovoltage modulate the secondary electron emission and

Y. Yalcinkaya, P. N. Rohrbeck, S. A. Weber
Max Planck Institute for Polymer Research
Ackermannweg 10, 55128 Mainz, Germany
E-mail: webers@mpip-mainz.mpg.de
Y. Yalcinkaya, S. A. Weber
Institute of Physics
Johannes Gutenberg University Mainz
Duesbergweg 10-14, 55128 Mainz, Germany
E. R. Schütz, A. Fakharuddin, L. Schmidt-Mende
Department of Physics
University of Konstanz
Universitätsstr. 10, 78464 Konstanz, Germany

The ORCID identification number(s) for the author(s) of this article can be found under https://doi.org/10.1002/adom.202301318

DOI: 10.1002/adom.202301318

thereby the image contrast. Irde et al.[25] have demonstrated the SEM-based mapping of SPV dynamics on methylammonium lead iodide thin films within seconds to hours.[25] Pietralunga et al.[26] used SEM-based SPV spectroscopy to study charge transport dynamics, internal electric field configurations, and interface energetics of perovskite films under illumination.[26] Generally, the irradiation with high-energy electrons under high vacuum conditions can damage delicate perovskite samples,[27] even though electron beam damage can be reduced via the use of low-energy electron beams[28] or by reducing the electron dose,[29] limiting the spatial resolution and the signal-to-noise ratio.[25,30]

Here, atomic force microscopy (AFM) is a more gentle and versatile alternative. Next to the sample topography, AFM can detect many other surface properties and sub-granular structures.[31–33] Using conductive AFM (C-AFM), Shao et al.[34] measured the current values on the perovskite grains and the GBs in between. These measurements demonstrated that ion migration is faster at GBs compared to grain interiors. Conings et al.[35] used C-AFM to track the degradation of methylammonium lead iodide films after annealing. Recently, we showed via C-AFM that an increased grain size as a result of methylamine treatment resulted in a higher conductivity and a lower charge accumulation at the GBs, indicating more efficient charge dissociation and transport within the grains. Another important AFM method is Kelvin probe force microscopy (KPFM). KPFM maps the electrostatic surface potential and has been used to reveal interfacial charges within perovskite devices[36–38] and band bending behavior at the GBs.[15,39] KPFM is particularly powerful in combination with sample excitation, for example, using voltage or light.[38,40] Since the contact potential difference (CPD) is depending on the electrostatic landscape on the surface, sample excitation by means of voltage or light pulses adds a modulation to the measured CPD value. Thus, KPFM can track charge carrier dynamics with high spatial resolution. Collins et al. carried out dynamic KPFM measurements by using general-mode KPFM (G-Mode KPFM)[41,42] to do fast KPFM measurements in the time range of tens of microseconds.[41] Other methods such as pump-probe KPFM (pp-KPFM)[43–46] can even locally resolve processes down to 1 ps.[43] Nevertheless, these methods require short excitation pulses at high repetition rates, limiting the application to fast and ultrafast processes (<µms).

In this study, we demonstrate KPFM-based nanoscale surface photovoltage spectroscopy (nano-SPV) and nanoscale ideality factor mapping (nano-IFM) as a tool to map the nanoscale distribution of defects. Using these methods, we investigate triple cation $Cs_{0.05}FA_{0.8}MA_{0.15}PbI_3$ perovskite films with different morphologies and surface passivation. We use nano-SPV to visualize the charge carrier dynamics at grains and GBs on perovskite half-cells with an architecture of (ITO/TiO_2-SnO_2/perovskite) with small, large, and PEA-passivated perovskite grains. Our nano-SPV measurements offer two types of measurement: i) tracking the SPV dynamics during and after a light pulse to track the extraction and recombination time of photo-generated charge carriers (nano-SPV) and ii) tracking the SPV as a function of light illumination to obtain the local ideality factor, n_{id} (nano-IFM). The results show suppressed ion migration when the number of GBs is lower due to large grains. Furthermore, half-cells showed more uniform and lower defect densities when the perovskite films were PEA-passivated or had larger grains.

2. Theory

Here, we introduce some common macroscopic SPV-based measurement methods and how we implement them in nano-SPV operation mode using KPFM.

2.1. Surface Photovoltage and Surface Photovoltage Decay

Upon illumination of a photovoltaic sample, the electrostatic potential on the surface will change. This SPV is commonly measured by means of a macroscopic Kelvin Probe. Here, a millimeter-sized metal plate mechanically vibrates above the sample. In the presence of a voltage difference between the plate and the surface, the periodic variations in the plate distance will lead to a capacitive current. By compensating the voltage difference via an external voltage, the capacitive current can be minimized. Already without external voltage, there is an intrinsic voltage difference called the contact potential difference (CPD). The CPD corresponds to the difference in work functions or the position of the Fermi Level, E_F, of the probe and the sample material:

$$V_{\mathrm{CPD}} = \frac{E_F^{\mathrm{tip}} - E_F^{\mathrm{sample}}}{e} \tag{1}$$

where e is the elemental charge. Any illumination-induced change in the measured CPD value corresponds to the SPV:

$$V_{\mathrm{SPV}} = V_{\mathrm{CPD,\,illum.}} - V_{\mathrm{CPD,\,dark}} \tag{2}$$

The SPV signal can have different contributions: i) band flattening at the semiconductor surface and ii) charge separation at buried interfaces. At the surface, defect states lead to Fermi-level pinning and band bending. The increased charge carrier concentration during illumination screens the trapped surface charges, leading to band flattening[47] (Figure S1, Supporting Information). The resulting change in the surface potential can be observed as a SPV signal, where the polarity depends on the majority charge carriers as in n- or p-type doping (Figure S1, Supporting Information). Typically, n-type semiconductors yield positive SPV while the SPV values are negative for p-type semiconductors. Therefore, the doping status of the sample can be estimated by the sign of the SPV value.[48]

On photovoltaic device stacks, a SPV signal can be caused by band bending at buried interfaces, for example, between the absorber and a charge-selective contact (Figure S2, Supporting Information). Here, photo-generated charge carriers redistribute across the heterojunction depending on the characteristics of the charge-selective layer. If the layer is an electron transport layer (ETL), the electrons will be transported while the holes remain within the semiconductor film and the resulting SPV will be positive due to the imbalance of free charges in the film volume.[26] On the contrary, if the charge selective layer is a hole transport layer (HTL), the electrons will remain in the absorber while the holes are transferred, leading to a negative SPV because of an excess of electrons.[26]

Since the SPV signal depends on the Fermi level and the Fermi level change under illumination in the sample, it is influenced by band bending, doping,[49] and stoichiometry in the sample.[50]

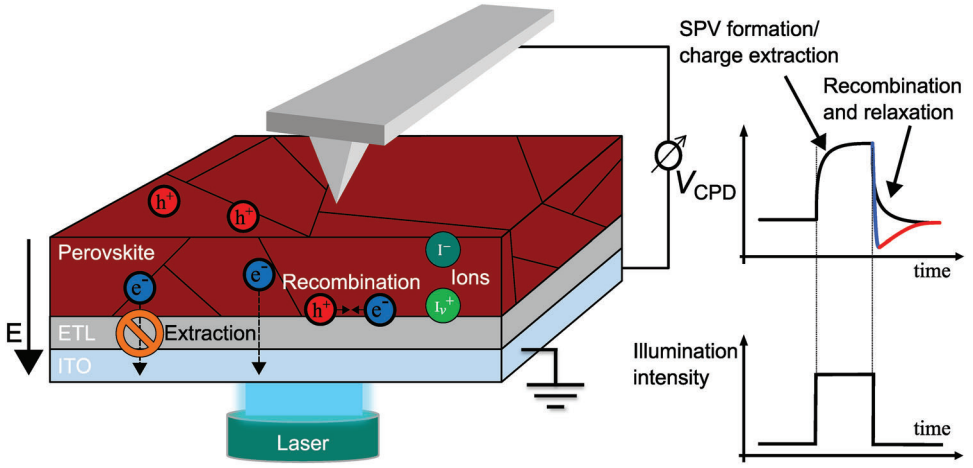

Figure 1. Schematic overview of the tr-KPFM setup. The laser intensity is either modulated in a pulse shape or a slow intensity increase with the tip engaged to the surface while the local CPD signal is recorded. The CPD traces contain information about local charge carrier extraction processes, which result in the formation of an electric field *E* (arrow on the left). After the light pulse, the CPD trace reveals information about recombination processes and the presence of defect states such as GBs and interfaces, which hinder the extraction of charges (blocking symbol).

To disentangle the different contributions to the SPV signal, we can track the SPV decay after an illumination pulse (SPV spectroscopy). The SPV transients contain information about recombination rates,[51] trap density,[52] and ion migration[40] effects. **Figure 1** shows the illustration of a SPV decay measurement result demonstrating the characteristic voltage decay following an illumination pulse. The decrease pattern gives information about the contributing charge carriers. The fast-decaying component (blue curve in Figure 1) is typically the electronic one whereas the slow-decaying one (red curve in Figure 1) is usually the ionic component.[40] The electronic decay is correlated to the electron–hole recombination mechanisms taking place at the perovskite bulk or the interface between the perovskite and the ETL after the illumination pulse. The more trap-assisted recombination occurs, the faster the SPV decay takes place. The ionic decay is correlated to the re-distribution of the ions from the surface which can be migrating from the crystal lattice or be adsorbed from the environment. Also, the electric field generated by the migration of electrons and the accumulation of holes at the surface influences the movement of ions within the film.

We further interpret the dynamics during the SPV formation at the beginning of a light pulse as the interfacial extraction of charge carriers. Other experimental studies using PL[53] or photoconductivity measurements came to a similar conclusion.[54] The results by Grill et al. suggest that only the ETL or HTL interface is the charge transport-limiting factor in the device and not the perovskite itself.[26,54] This means it is possible to see interfacial proprieties of the device by tracking the change of the SPV.[26]

2.2. Ideality Factor

The current–voltage (*I*–*V*) characteristics of semiconductor diodes such as solar cells can be described by the Shockley diode equation:

$$I = I_L - I_S\left(e^{\frac{V}{n_{id}k_BT/q}} - 1\right) \tag{3}$$

where I is the overall current of the solar cell, I_L is the light-generated current, I_S is the reverse bias saturation current, V is the voltage across the solar cell, k_B is the Boltzmann constant, T is the temperature, and q is the elementary charge. Here, the ideality factor, n_{id}, is a measure of how close a photovoltaic device behaves to an ideal diode ($n_{id} = 1$). Deviations from the ideal diode behavior can be caused by charge carrier recombination mechanisms. Here, n_{id} can be estimated as the relation between the quasi-Fermi-level splitting, ΔE_F, and the recombination rate, R[55]:

$$n_{id,C} = \frac{1}{kT}\frac{d\Delta E_F}{dln(R)} \tag{4}$$

where $n_{id,\,C}$ is the conceptual ideality factor and kT is the thermal energy. Typically, a higher n_{id} suggests that the traps within the semiconductor contribute to the recombination process more.[56] Practically, it is hard to obtain values for the recombination rate and local quasi-Fermi level splitting values independently to obtain $n_{id,\,C}$. To work around this obstacle, an approximate value for n_{id} can be estimated from the current and voltage of the device. Here, the dark current, J_d, replaces the recombination rate, whereas the external voltage, V_e, replaces the local quasi-Fermi level splitting to obtain dark ideality factor, $n_{id,\,d}$, in Equation 5:

$$n_{id,d} = \frac{q}{kT}\frac{dV_e}{dln(J_d)} \tag{5}$$

This equation uses easily measurable quantities to obtain n_{id}. Nevertheless, this approach has the disadvantage that shunt or series resistances contribute to the ideality factor, as well as the recombination rates. Therefore, the $n_{id,\,d}$ can give misleading results.

At open circuit conditions under illumination, charge generation and recombination rates are equal, as the net charge extraction is zero. Here, the steady-state open-circuit voltage (V_{oc}) can be seen as an approximation of the quasi-Fermi level splitting.

By measuring V_{oc} as a function of light intensity, ϕ, we can vary the recombination/generation rate within the device. Modifying Equation 6 yields

$$n_{id,l} = \frac{q}{kT}\frac{dV_{oc}}{dln(\phi)} \tag{6}$$

which we refer to as the light ideality factor, $n_{id,l}$. This value gives information about the recombination mechanisms with a minimum contribution from series or shunt resistances. Thus, a comparison of the $n_{id,l}$ values between samples allows for determining the degree of trap-assisted recombination.[57] Nevertheless, there is an ongoing debate about the interpretation of n_{id} in PSC devices. Recently, Caprioglio et al.[58] reported on optical n_{id} measurements on half and full perovskite solar cells with different perovskite/transport layer interfaces and compared the n_{id} values. Their work suggests that the interfacial recombination dominates in n_{id} over the bulk recombination contribution.

2.3. Static and Time-Resolved Kelvin Probe Force Microscopy

The methods discussed so far rely on macroscopic measurements, for example, using a millimeter-sized Kelvin probe or an optical excitation spot.[59] KPFM is an AFM-based adaptation of the Kelvin probe measurement principle.[60–63] Instead of a capacitive current, KPFM detects the electrostatic force caused by the tip-sample potential to quantify the CPD. KPFM-based CPD maps can give information about facets,[64] band bending due to defects,[65] and energy level alignment in solar cells.[38]

To both map and record the nanoscale CPD and SPV dynamics with KPFM, the conventional scanning mode would be too slow. We recently introduced a point-wise time-resolved KPFM (tr-KPFM) data acquisition method where we record the sample response to a light or voltage pulse subsequently on every pixel of an image (Figure 1).[38,66] Here, we collect the CPD dynamics upon light or bias excitation subsequently at individual pixels within a designated area of the sample. Once the whole map is completed, we can either extract snapshots of the CPD distribution at defined positions in time or extract traces of CPD dynamics at defined positions in space (see also Experimental Section for more details). This method has the advantage that it is not limited in terms of the duration of the CPD traces. In particular, on PSC samples, where the full ionic relaxation can take several hundreds of milliseconds,[38] it is important to wait long enough to allow the sample to relax back to an equilibrium state. Other dynamic KPFM methods[41–46,67] require an excitation at high repetition rates, which might leave the sample effectively in an excited state. Thus, using only standard KPFM equipment (lock-in amplifier and feedback system), tr-KPFM can map the CPD and SPV distribution in the time scale of hundreds of microseconds to seconds. We call this operation mode nano-SPV.

Although flexible in terms of longer timescales, there are physical restrictions in terms of the shortest timescales that can be detected with tr-KPFM and nano-SPV. In the heterodyne KPFM detection mode used in this study,[68,69] signals are detected by means of an amplitude change on one of the cantilever's resonances. Therefore, the smallest detectable time scale τ_{min} is determined by the damping or Q-factor on this resonance:

$$\tau_{\min,\,n} = \frac{Q_n}{f_n \cdot \pi} \tag{7}$$

where Q_n and f_n are the Q-factor and frequency of the n-th resonance of the AFM cantilever, respectively (see Experimental Section and Section S2, Supporting Information, for details). For a typical cantilever used in this study with second eigenmode frequency f_2 = 977 kHz and Q_2 = 461, the smallest timescale is, therefore, τ_{lim} =150 µs. This limit could be further pushed by using cantilevers with higher resonance frequency, or by using frequency modulation detection.

3. Results and Discussion

To investigate the correlation between sample structure, surface treatment, and defect distribution in perovskite thin films, we prepared triple cation perovskite films with 0.95:1.05 A^+/B^{2+} cation ratio with different structures (see Experimental Section for details). The topography images obtained via AFM are shown in Figure S3 in Section S4, Supporting Information. These include: i) a reference sample with small ($<d>_{Ref}$ = 200 ± 60 nm) grains (Ref), ii) a dimethyl sulfoxide (DMSO) vapor solvent annealed ($SA_{Pristine}$) ($<d>_{SA_{Pristine}}$ = 590 ± 160 nm), iii) solvent-annealed triple cation sample with PEA-I surface passivation (SA_{Pass}) ($<d>_{SA_{Pass}}$ = 670 ± 210 nm), and iv) a methylamine gas-treated triple cation sample with large ($<d>_{MA80}$ >100 µm) grains (MA80). By comparing the reference perovskite film to the solvent vapor-annealed and/or passivated perovskite films, we aim to identifying surface structures with locally higher or lower defect concentrations.

3.1. Reference Sample

The topography on the reference sample (**Figure 2a**) shows a structure of grains with a size of $<d>_{Ref}$ = 200 ± 60 nm. The correlated equilibrium CPD map before the voltage pulse (Figure 2b) mostly shows the contrast between the grains and the GBs due to band bending at the GBs,[15] where CPD increase and decrease correspond to downward and upward band bending, respectively. The CPD varies at the GBs within a range of 2 to 30 mV (Figure S4, Supporting Information). Furthermore, most GBs show higher CPD values compared to the grain interiors with minor exceptions (Figure S4e, Supporting Information). Since the band bending direction is determined by the type of defects, we argue that the minority GBs that show smaller CPD compared to the grains indicate different type of defects compared to the rest of the GBs within the film. Apart from that, some grains exhibited around 240 mV lower CPD value than the rest of the image (average value of 760 ± 90 mV). By subtracting the CPD values before illumination from the CPD values during illumination, we obtained a map of the SPV distribution (Figure 2c). The illumination pulse (0 ms $< t <$ 201.6 ms) resulted in an average photopotential of 280 ± 90 mV. Interestingly, grains with initially lower CPD exhibited about 190 mV higher SPV compared to the rest of the sample. The heterogeneous distribution of the SPV

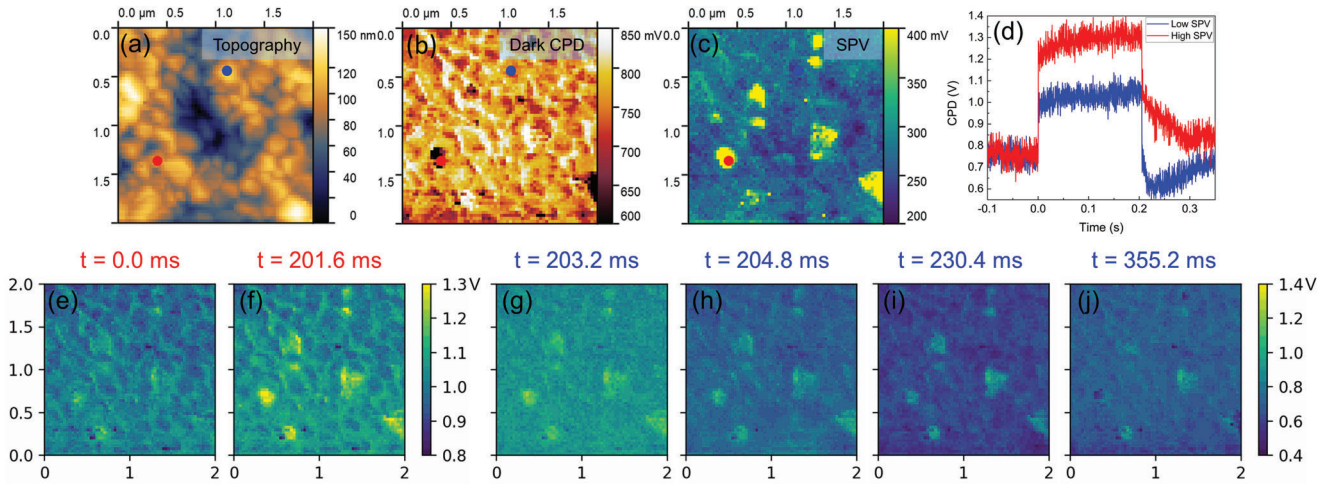

Figure 2. a) Topography, b) CPD in dark, c) SPV, and d) SPV plots over time from marked areas of reference perovskite sample. Panels (e)–(j) show the CPD maps at different time frames. The maps have 150x150 pixels.

suggests either non-uniform defect distribution or non-uniform chemical stoichiometry within the reference perovskite film. The former possibility would be causing changes in the local Fermi levels, whereas the latter would change the Fermi level shift during illumination.[50]

When comparing the dynamics at high and low SPV areas (Figure 2d; red and blue markers in Figure 2c and Figure S5b, Supporting Information), the SPV decay at the high SPV grain shows a slower decay compared to SPV decay at the low SPV grain (Figure 2d). Furthermore, the SPV decay at the blue marker shows a rapid decrease to negative SPV values before returning to the equilibrium dark CPD value. This undershoot could be caused by ion migration as illustrated in Figure 1.[40] During illumination, the electric field caused by the SPV polarizes mobile ions within the perovskite layer. After the illumination, the electronic polarization rapidly decays, leaving behind the ionic field that generates a negative surface voltage. The slower SPV decays within the high SPV grain (red and orange markers) suggest that the defect density is lower at the high SPV areas of the reference sample. Furthermore, the absence of an SPV undershoot during decay also suggests that the ion migration is suppressed at the high SPV areas.

The snapshots of the CPD distribution of the reference perovskite film at different times during the nano-SPV measurement show the time-evolution of the SPV before (Figure 2b), during (Figure 2e,f), and after (Figure 2g–j) the illumination pulse (see also Video S1, Supporting Information). Directly after the laser was switched on, the CPD distribution remained rather uniform at 1030 ± 40 mV; 200 ms later, the contrast between the low and high SPV grains was clearly visible. Directly upon switching off the laser, the CPD values started to decrease due to the charge carrier recombination (Figure S6, Supporting Information). The electronic recombination for most of the image occurred within the first ≈30 ms after the laser was switched off (Figure 2i) at which the average CPD reached a minimum (Figure S6, Supporting Information). After reaching the minimum, the average CPD of the whole map increased again due to the slow decay of the ionic polarization that occurs in low SPV areas (blue plot in Figure 2d), and most grains relaxed back to their original dark CPD values (Figure 2j). The high SPV grains, however, showed longer decay times without the ionic undershoot, as also shown in Figure 2d. The absence of ionic polarization and the longer SPV decay time suggest that the defect density is lower at the high SPV areas of the reference sample.

3.2. Solvent-Annealed Pristine Sample

To investigate the effect of solvent annealing on the defect density, we prepared triple cation perovskite films with a post-treatment of DMSO solvent annealing. This post-treatment should lead to a better crystallinity of larger grains and decreased GB density.[70] It also has been shown that the larger grain size reduces the defect density within the perovskite layer.[71] The topography of the $SA_{Pristine}$ sample (**Figure 3a**) showed larger perovskite grains ($\langle d \rangle_{SA_{Pristine}} = 590 \pm 160$ nm) compared to the reference ($\langle d \rangle_{Ref} = 200 \pm 60$ nm) due to the solvent annealing.[72] The dark CPD picture of $SA_{Pristine}$ can be found in Figure S16 in Section S6, Supporting Information. The distortions in the form of comb-like artifacts were caused by sample drift.

The nano-SPV map of the $SA_{Pristine}$ sample (Figure 3b) shows a pattern that matches some features in the topography map. The ETL of the reference sample and the $SA_{Pristine}$ are SnO_2 and c-TiO_2, respectively (see Experimental Section). Nevertheless, compared to the reference, the SPV value decreased slightly, from 280 ± 90 to 210 ± 50 mV on the $SA_{Pristine}$ sample. This lower SPV signal could be the result of a reduced band bending at the top surface due to the improved film quality[73,74] or a reduced charge transfer at the ETL interface, for example, due to energy barriers. Furthermore, at some of the GBs, we observed a stronger SPV contrast compared to the reference sample (SPV profiles in Figure S12b, Supporting Information). These profiles reveal a 73 ± 15 mV lower SPV at the GB compared to the grain interior. This value is in agreement with previous reports.[15] The lower SPV at the GBs could be caused by band bending at the GBs.[48] Furthermore, we see a SPV contrast of about 32 ± 5 mV between

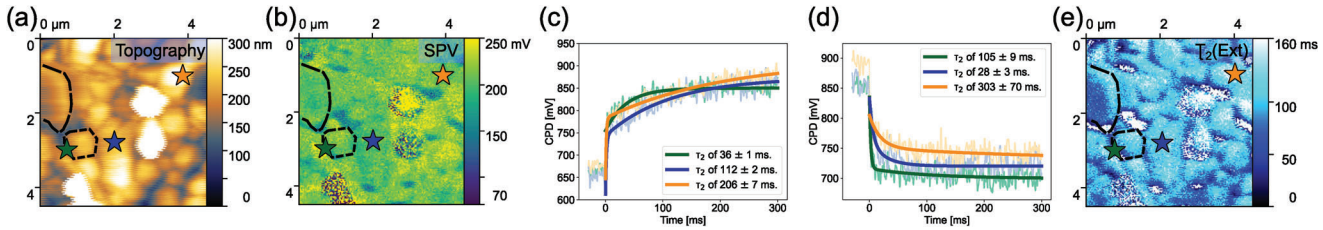

Figure 3. a) The topography; b) SPV map; c) CPD spectroscopy curves with 30 ms pre-zero data of spots marked in (a), (b), and (e) with a calculated slow timescale of electron extraction (τ_2(extraction)) in respect to turning on the laser; d) CPD spectroscopy curves with 30 ms pre-zero data of spots marked in (a), (b), and (e) with a calculated slow timescale of electron recombination (τ_2(recombination)) in respect to turning off the laser; and e) SPV rise time τ_2(ext) map of $Cs_{0.05}FA_{0.8}MA_{0.15}PbI_3$ perovskite film with 0.95:1.05 A/B cation ratio ($SA_{Pristine}$). An extended version is available in Figures S7–S9, Supporting Information.

some individual grains and even within the same grain (see Figure S13b,c, Supporting Information). These differences could result from a facet dependency of the SPV,[75] stochiometry differences, or the defect distribution within the perovskite film. The elevated structures that are visible in the topography (Figure 3a) and the corresponding noisy SPV features in Figure 3b, together with a locally lower CPD (Figure S16, Supporting Information) could be caused by a locally higher PbI_2 concentration.[15]

We further analyzed the nano-SPV dynamics in different locations on the map with similar SPV values. One spot was chosen to be on a GB (green star) and two were placed within different grains (blue and orange stars in Figure 3a,b,e). Analyzing the SPV decay curves, it is obvious that the ionic undershoot that we observed on the reference sample disappeared on most grains in Figure 3d (some exceptions are shown in Figure S7 in Section S6, Supporting Information). The suppression of ion migration[40] is a result of the increased grain size and fewer GBs.[74,76] We want to point out that the increase in the grain size already had a massive impact on the ion migration. This means increasing the grain size alone already improves the defect density at the GBs. Although the grains marked with blue and orange stars exhibited a similar SPV value, the timescale until the SPV reached equilibrium varied from 112 ± 2 to 206 ± 7 ms, respectively. On the GBs, these timescales were even shorter ~36 ± 1 ms ($<\tau_2$(ext)$>$(GB)$_{SA_{Pristine}}$ = 64 ± 21 ms; $<\tau_2$(ext)$>$(grain)$_{SA_{Pristine}}$ = 300 ± 30 ms; see also Video S2, Supporting Information). Changes of SPV in the time range of seconds have been reported before by tr-SEM measurements[25] and by earlier tr-KPFM measurements on device cross sections.[77,78]

Since ion migration is suppressed in solvent-annealed samples, the SPV decay is dominated by electron–hole recombination. Therefore, the shorter decay at the GBs can be attributed to faster electron–hole recombination, which points out higher defect density at the GBs. We interpret the equilibration time of the SPV as a local capacitive charging or extraction time, where the photogenerated charges fill up the capacitor between the bottom contact and the perovskite surface. Here, a faster equilibration time is indicative of a higher generation rate or a lower capacitance of the perovskite material. Moreover, the recombination or discharging traces and, therefore, the time in Figure 3d also show a wide variation of τ_2(rec) values between 28 ± 3 and 303 ± 70 ms. We did not observe a consistent correlation between the extraction and recombination times, indicating that the mechanisms of charge extraction and charge recombination are different. This is up to future research.

The fact that the nano-SPV measurements yield complete SPV traces for every position on the samples allows for generating maps of the equilibration timescales. We were able to fit most of the nano-SPV traces for excitation (ext) and recombination (rec) with a double exponential fit, indicating that two distinctly different timescales, τ_1 and τ_2, are involved in the dynamics. While all the other timescales showed no clear contrast, we found a distinct contrast between the grain interior and the GB in τ_2(ext) (see Figure 3e). Furthermore, there is a weak correlation between the SPV magnitude and the SPV extraction time that could be connected to different crystal facets. Generally, we observed higher SPV extraction times for lower SPV grains or grain facets, for example, the area in Figure 3b right to the long dotted line marked grain. This area had a lower SPV, but a higher extraction time in Figure 3e. This contrast trend could originate from stoichiometric differences or variations in defect density between grains in the triple cation perovskite film. The difference of τ_2(ext) between the grain interior and the GB is about 33 ± 6 ms (see Figure S14b, Supporting Information). This observation demonstrates that the extraction of charge carriers usually takes place much faster at GBs compared to the grain interior.

Although Regalado-Pérez et al. have suggested poor electronic transport due to local electric fields at GBs caused by an accumulation of negatively charged ionic defects,[74] Tainter et al. performed bulk measurements of photocurrent at excitation-junction separations much larger than topographical feature size and find that large fractions of excited carriers travel across multiple GBs.[79] These authors assumed that GBs do not prevent charge diffusion and GBs are not major impediments to charge motion in the polycrystalline films.[79–81] Moreover, Shao et al. saw that larger grains have GBs perpendicular to the substrate.[82] We, therefore, think that the overall increase in the grain size due to the DMSO vapor annealing has not only improved the crystallinity of the film but also made the GBs fast perpendicular pathways to the underlying substrate. Such a conductive pathway would explain the faster dynamics that we observed at the GBs with nano-SPV. Furthermore, Figure 3e shows not only a difference between the grain interior and the GB but also shows a facet dependence of the timescale of the nano-SPV response (e.g., the top left grain marked with a dashed line in Figure 3a,b,e and Figure S7a–d, Supporting Information).

Comparing the map of extraction/generation time constants (Figure 3e) to the map of the fast recombination/decay timescale in Figure S18, Supporting Information, we see a similar pattern. In particular, positions where the SPV stabilized fast were also

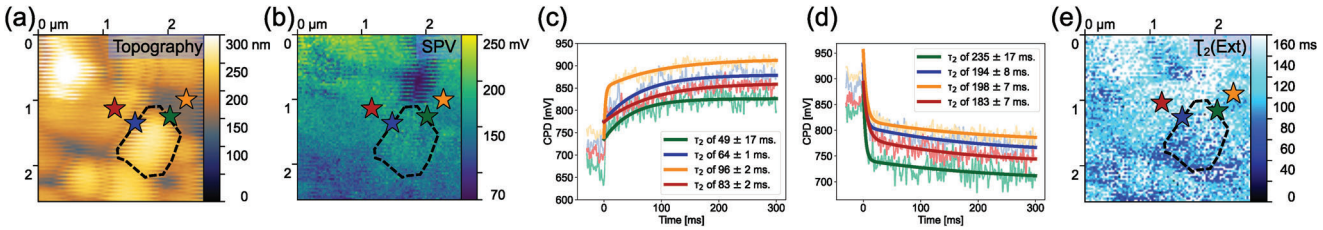

Figure 4. a) The topography; b) SPV map; c) CPD spectroscopy curves with 30 ms pre-zero data of spots marked in (a), (b), and (e) with a calculated slow timescale of electron extraction (τ_2(extraction)) in respect to turning on the laser; d) CPD spectroscopy curves with 30 ms pre-zero data of spots marked in (a), (b), and (e) with a calculated slow timescale of electron recombination (τ_2(recombination)) in respect to turning off the laser; and e) SPV rise time τ_2(ext) map of $Cs_{0.05}FA_{0.8}MA_{0.15}PbI_3$ perovskite film with 0.95:1.05 A/B cation ratio and surface passivation (SA_{Pass}). A combined figure of the CPD spectroscopy trajectory shown in (c) and (d) can be found in Figure S24, Supporting Information.

positions with fast SPV decay after the light was switched off. Interestingly, the second timescale obtained from the fits was very long, up to 1.5 s (see Figure S19, Supporting Information). Mapping the longer timescale, we observed a much more homogeneous contrast. Nevertheless, the exact meaning of this second timescale remains unclear and will be subject to future studies.

3.3. Solvent-Annealed and Passivated Sample

The topography of the SA_{Pass} sample **Figure** 4a shows slightly larger perovskite grains ($\langle d \rangle_{SA_{Pass}} = 670 \pm 210$ nm) compared to the $SA_{Pristine}$ sample (Figure 3a). Again, the comb artifacts are caused by sample drift and should not affect the interpretation of the results. The dark CPD picture of SA_{Pass} can be found in Figure S28 in Section S7, Supporting Information.

The nano-SPV image (Figure 4b) shows a more uniform distribution compared to the SPV image of the $SA_{Pristine}$ sample (Figure 3b). Overall, the SPV value decreased from 210 mV with an RMS variation of 50 mV on the reference sample to 160 mV with an RMS deviation of 30 mV on the passivated sample. The decrease of the SPV could be the result of less band bending (shown in Figure S1, Supporting Information) due to the passivation of surface defect states. Furthermore, the grain–GB contrast decreased as a result of the passivation. The dark CPD decreased probably due to the site-specific passivation of the GBs by forming a 2D perovskite.[15] The lower defect density due to the passivation specifically at the GBs may lead to decreased band bending (see Figure S1, Supporting Information). This causes the SPV to be lower since there is less energy needed to flatten the bands.

To further support the homogeneous distribution of the passivation agent, we analyzed again four spots on the SA_{Pass} sample with similar SPV values (see spots in Figure 4b) on GBs and within grains. Figure 4c shows that the curves appear much more similar compared to the $SA_{Pristine}$ (Figure 3c,d). The values of τ_2(ext) are only separated by about ≈23 %. The SPV extraction time map of SA_{Pass} given in Figure 4e shows an overall improved SPV extraction time uniformity compared to the $SA_{Pristine}$ sample (see Figure 3e and Video S3, Supporting Information). There is a medium intergranular difference of τ_2(ext) of ≈20 ms between the grains shown in Figure 4e. Similar to the pristine perovskite film, the fast recombination time map (see Figure S30, Supporting Information) shows a uniform distribution (Figure 4a). Some non-uniformity could be caused by the non-homogeneous distribution of PEA-ions on the surface during preparation. Nevertheless, the distribution is much more homogeneous compared to the pristine one (Figure S18, Supporting Information). Slower SPV recombination times usually indicate slower recombination[83] due to the passivation. Therefore, our results show that surface passivation with PEA leads to a more uniform SPV distribution and SPV extraction time behavior on GBs and within grains due to the homogenized defect density within the perovskite film and/or the formation of 2D-perovskite phases shown in a previous study.[15]

3.4. Methylamine-Treated Sample

The topography image of the MA80 sample (**Figure** 5a) shows a structure where the grain size exceeds 100 µm. Due to the limited scan size of the AFM, we were not able to investigate areas with several grains and therefore focused on one particular GB (diagonal line from top left to bottom right in Figure 5a). The CPD map before the illumination (Figure 5b) shows grain–GB contrast without any contrast within grains with no topographical features. The average dark CPD was 960 ± 50 mV within the grains with and about 65 mV higher at the GBs. The SPV map (Figure 5c) obtained during the illumination pulse (0 ms $< t <$ 201.6 ms) shows an average SPV of 200 ± 40 mV with an ≈60 mV lower value at the GB. The fact that the CPD and SPV contrast are almost identical at the GBs supports the notion of band bending at the GBs that we suggested previously. Apart from the GBs, MA80 shows uniform behavior considering both CPD and SPV distribution. Therefore, we suggest that methylamine treatment heals the perovskite grains and homogenizes the stoichiometry, leading to a more uniform CPD and SPV distribution.

To investigate the nano-SPV dynamics at high and low SPV areas (Figure 5c, blue and red markers, respectively), we looked at the SPV traces located at the grain interiors and a GB, respectively (Figure 5d, blue and red markers in c, respectively). The SPV dynamics upon excitation were comparable to those of the previous samples. Surprisingly, we observed a spike (inset of Figure 5d) in CPD about 3 ms after the light was switched off. Such a V_{OC} overshooting effect has also been reported by Herterich et al. during solar cell device measurements.[84] These authors suggested that due to the presence of mobile ions in the perovskite layer, a space charge layer forms between the perovskite and the contact layer. This space charge layer decreases the conductivity of the majority charge carriers, leading to a gradient of the quasi-Fermi level splitting at the contact interface. When the light is switched

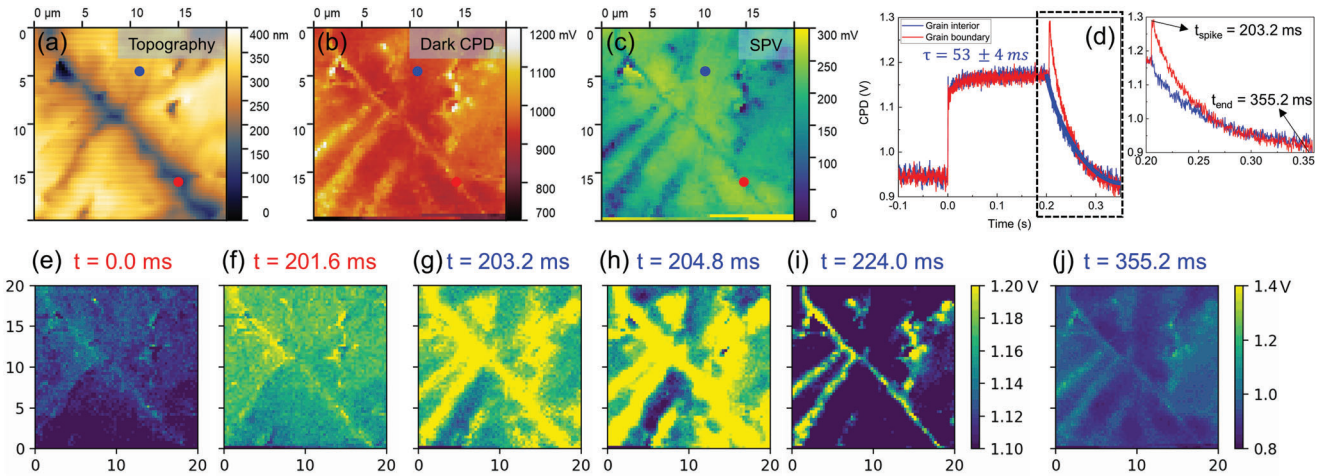

Figure 5. a) Topography, b) CPD in dark, c) SPV, and d) SPV plots over time from marked areas of the MA80 sample. Panels (e)–(j) show the CPD maps at different time frames. The maps have 150x150 pixels.

off, this gradient at the interface decreases faster compared to the bulk quasi-Fermi level splitting, resulting in V_{OC} overshoot.

When we examine a nano-SPV trace within a grain, we see a SPV decay without any overshoot. Furthermore, in both grain and GBs, the decay shows longer SPV decay times compared to the reference sample. The SPV decay given in Figure 5e decays with a characteristic time of 53 ± 4 ms according to the double exponential fit of the signal. This result is also backed by our previous observations on MA gas-treated samples.[85] The longer charge recombination times in both tr-PL (Figure S38, Supporting Information) and SPV decay (Figure 5d) indicate reduced defect density of the MA80 film due to the healing effect of methylamine treatment and fewer GBs. The increased crystallinity and grain orientation that we observed from the XRD patterns (Figure S36, Supporting Information) is possibly a contributing factor that leads to increased charge recombination times. The PL spectra given in Figure S37a, Supporting Information, also support the improvements that we see in SPV and XRD results, since the PL full-width half maximum is narrower after the methylamine treatment. The absence of a SPV undershoot further supports our earlier conclusion that decreasing the number of GBs further suppresses ion migration within the perovskite.

The SPV time frames gathered from the MA80 film during the nano-SPV experiment show the CPD distribution before (Figure 5b), during (Figure 5e,f), and after (Figure 5g–j) light illumination (see also Video S4, Supporting Information). When the laser was first switched on, the CPD had an average value of 1130 ± 50 mV, while it evolved to an average of 1160 ± 20 mV within 200 ms (Figure 5e,f). After switching off the laser, the CPD within the grains started to relax back to the original values due to charge carrier recombination. The SPV maps revealed that the SPV overshoot within the first 3 ms after the light pulse had a magnitude of up to 120 mV in the vicinity of the GB. This overshoot leads to a SPV decay contrast between the perovskite grains and the GBs, comparable to the dark CPD distribution. The SPV overshoot contrast between the GB and the grains suggests that the ion accumulation at the interface is higher at GBs. At the end of the nano-SPV recording at t = 355.2 ms, we see that the CPD image is almost identical to the dark CPD image. This suggests a more uniform SPV decay behavior within the grains of the MA80 film compared to the reference film. Moreover, the absence of CPD contrast within the grains suggests that the methylamine treatment could be working as a passivation treatment by healing the A^+-cation site defects or causing uniform chemical stoichiometry distribution throughout the film.

3.5. Nanoscale Ideality Factor Mapping

As we have shown, CPD and SPV measurements can be used to map sample heterogeneity in terms of Fermi level contrast and SPV decay times, which are mainly related to defects. However, the changes in these parameters could be linked to local stoichiometry changes[50] as well as they could be linked to the presence of defects within the perovskite layer or at the interfaces. Furthermore, the time resolution of tr-KPFM during SPV decay is determined by the use of our cantilevers and is in the order of 0.-1-1 ms. This limitation makes it difficult to obtain quantitative results from samples with shorter SPV decay times (Figure 2j). Therefore, we introduce a new KPFM-based technique where we locally measure the recombination behavior in the semiconductor film by measuring the $n_{id,l}$ of our perovskite half-cells named nano-IFM. To use the concept of $n_{id,l}$ to our advantage, we used our AFM tip as a nanoscale probe for each pixel and measured the SPV as a function of illumination intensity. By doing so, we are able to map the $n_{id,l}$ in the scan area of the sample (see Section S10, Supporting Information).

The topography image (**Figure 6**a) shows the granular structure of the same reference perovskite film given in Figure 2. The grain size varied between 100 and 400 nm. The SPV map shows an average SPV of 110 ± 20 mV (Figure 6b). Some grains show higher SPV values up to 200 mV compared to the rest of the sample. Furthermore, SPV values decreased between 10 and 20 mV at the GBs. As we suggested previously, the SPV contrast could be related to the stoichiometry or defect density distribution within the reference perovskite film. The $n_{id,l}$ distribution within the grains shows the same trend as the SPV distribution, where the

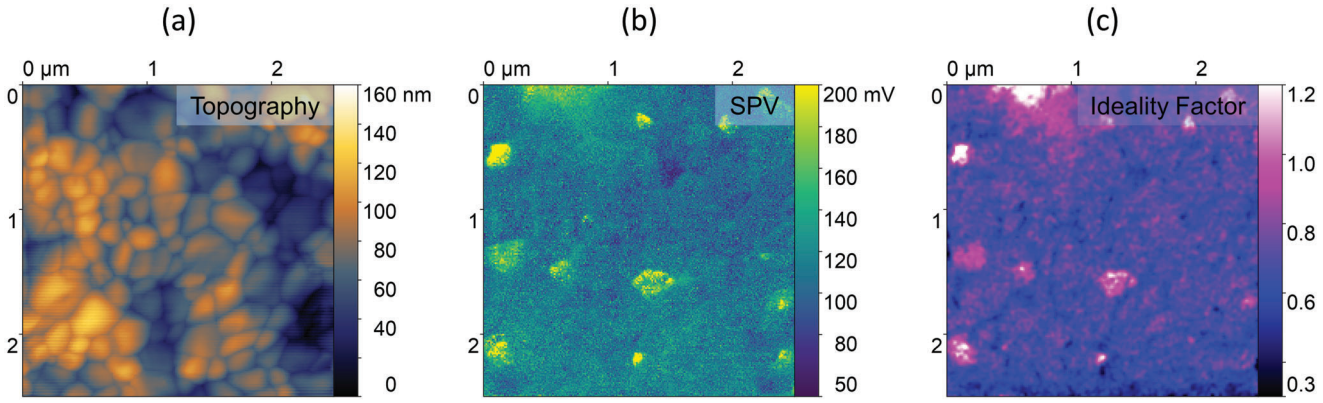

Figure 6. a) Topography, b) SPV, and c) $n_{id,\,l}$ maps of reference perovskite film. The map contains 200x200 pixels. The nano-IFM map was 1x1 pixel Gaussian filtered.

average $n_{id,\,l}$ value is 0.69 ± 0.11, with up to 0.3 higher $n_{id,\,l}$ values within the grains with higher SPV in Figure 6b, suggesting that these grains exhibit a lower defect density (Figure 6c). Thus, we conclude that the defect density at the grain interiors is not uniform within the perovskite film, in agreement with the earlier interpretation of the SPV decay (Figure 2a–f) and SPV distribution (Figure 2h). Moreover, this result also suggests a direct correlation between the quasi-Fermi level splitting and the $n_{id,\,l}$, which demonstrates the dominance of interfacial recombination in our perovskite half-cells.[58,59] The GBs in Figure 6d show lower $n_{id,\,l}$ values between 15 and 20 compared to the grain interiors, which points out the higher defect density at the GBs.

On the MA80 sample, we again focused on a region with a GB (Figure 5g). Here, we observed two GBs: the crack-like boundary on the left and the more subtle boundary on the right (**Figure** 7a). Apart from these boundaries, the topography was smooth with 36 nm RMS roughness (Figure 7a). The SPV map (Figure 7b) shows a uniform distribution within the grains with an average value of 370 ± 50 mV and about 20 mV lower SPV values at the GB. However, SPV values of the grains near the GB were about 50 mV higher compared to the average SPV. The features appearing in these areas in the dark CPD map (Figure S42b, Supporting Information) suggest that this effect could be related to a stoichiometric change. The $n_{id,\,l}$ map, like the SPV map, shows uniform distribution within the MA80 film with an average value of 0.92 ± 0.28 (Figure 7c). Some areas within the grains show an about 0.4 lower n_{id}, value compared to the average value. This decrease could be related to the topographical features (Figure 7a). The grain–GB contrast in Figure 7d exhibits a $n_{id,\,l}$ drop of around 0.1 at the GB. This shows that the GBs still possess higher defect density, even after the methylamine treatment. Interestingly, the SPV contrast (Figure 7b) and the $n_{id,\,l}$ contrast (Figure 7c) do not exactly overlap. This supports our previous notion that SPV increases near the GBs are caused by the chemical stoichiometry changes. Therefore, a comparison of the SPV and the $n_{id,\,l}$ maps can give us stoichiometry and defect contrasts within the same film after a single nano-IFM measurement.

Comparing the overall $n_{id,\,l}$ values of the measured films, we see that the average $n_{id,\,l}$ increased after the methylamine treatment from 0.69 ± 0.18 to 0.92 ± 0.28. Therefore, our nano-IFM results suggest that the methylamine treatment increases the grain sizes and decreases the defect density inside the grains. The non-conventional $n_{id,\,l}$ values below 1 could be related to the fact that the measurements are carried out on perovskite half-cells with ITO/ETL/perovskite structure in which there is a charge carrier imbalance due to the absence of an HTL layer. Previously, $n_{id,\,l}$ values below 1 have been reported to be caused by energy misalignment between the absorber layer and the HTL in organic

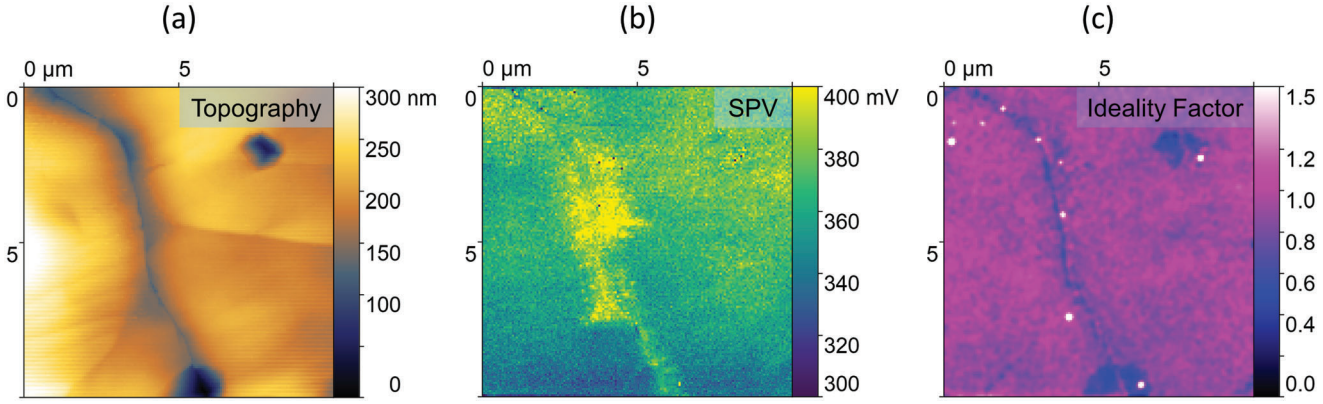

Figure 7. a) Topography, b) SPV, and c) $n_{id,\,l}$ maps of MA80 film. The map contains 150x150 pixels. The $n_{id,\,l}$ map was 1x1 pixel Gaussian filtered.

solar cells.[86] Also, the effect of ion migration and the possible space charge layers at the interfaces on $n_{id,l}$ is not entirely clear in the classical diode theory.[87] The quantities obtained via nano-IFM could be the subject of future research.

4. Conclusion

Using nano-SPV and nano-IFM, we demonstrate the effect of GBs on the lateral defect distribution in triple-cation perovskite films. Using pulsed and ramped laser illumination during tr-KPFM measurements, we showed the occurring changes within the perovskite films with small grains, large grains, and passivated grains. These measurements enabled us to experimentally demonstrate the effect of chemical processing on the nanostructures and charge carrier dynamics within the halide perovskite devices. Fewer GBs within the perovskite film lead to longer SPV lifetimes, which agrees with longer electron–hole lifetimes as observed in tr-PL. Furthermore, the ion migrations within the perovskite films were suppressed in solvent-annealed ($SA_{Pristine}$ and SA_{Pass}) and MA80 films due to a lower density of GBs and higher crystallinity. The nano-SPV and SPV decay maps showed more uniformity when defects were passivated via PEA coating. Also, the nano-SPV map showed that the MA80 film shows a more uniform SPV distribution compared to the reference perovskite film. We furthermore showed the different recombination behavior of reference and MA80 perovskite films by nano-IFM. Our $n_{id,l}$ mapping results show that different GBs can show varying recombination mechanisms but they are still the main locations for trap-assisted recombination within the perovskite films. According to our results, the negative effects of GBs are suppressed by surface passivation. On top of that, the grain interiors are also positively affected by the passivation agent coating as the higher SPV decay values measured in the grains suggest. Nevertheless, even the optimized films still exhibited some lateral variations in the defect density, thus guiding the way for targeted optimization of perovskite solar cells. Our results highlight the potential of nano-SPV and nano-IFM for the investigation of nanoscale structure–function relationships in optoelectronic materials beyond perovskites.

5. Experimental Section

Preparation of Perovskite Films: The planar ETL/perovskite half solar cells had the architecture of ITO/c-TiO_2/$Cs_{0.05}FA_{0.8}MA_{0.15}PbI_3$.

The triple-cation perovskites ($Cs_{0.05}FA_{0.8}MA_{0.15}PbI_3$) used for the tr-KPFM measurements were prepared on Ossila ITO-coated glass substrates with a conductivity of 20 Ω. After being brushed with Hellmanex III (Hellma), the ITO substrates were washed with hot tap water and milliQ water and then dried with an air gun. Afterward, the ITO substrates were treated with UV–ozone for 30 min freshly before the preparation of the compact TiO_2 (c-TiO_2) and once more before the perovskite layer. The c-TiO_2 layer was prepared by spin coating 80 µL of a 0.75 mol L^{-1} aqueous $TiCl_{4(aq)}$ solution on the ITO glass. The substrates were dried for 5 min @ 100 °C and then heated for 30 min on a high-temperature hot plate at a temperature of 500 °C. The perovskite precursor solution of 1.0:1.0, 0.9:1.1, and 0.8:1.2 A^+:B^{2+} cation ratio were prepared each with the concentration of 1.3 mol L^{-1} for PbI_2 in DMSO: *N*,*N*-dimethylformamide (DMF) (both anhydrous, Sigma-Aldrich) in a 1:4 volume ratio (v:v). For spin coating, 100 µL of the perovskite precursor solution was placed on the substrate and spin coated for 10 s @ 1000 rpm followed by 20 s @ 6000 rpm. 5 s before the end of the second step, 200 µL of chlorobenzene (CB) was used as an antisolvent. The substrate was then put on a hot plate with a temperature of 100 °C first until the substrate turned black and the film dried completely (≈10 s) and then for 15 min in an atmosphere of DMSO under a petri dish for solvent annealing. For each six samples, one petri dish was used with 90 µL of DMSO. The solvent annealing step was followed by a step of thermal annealing at 100 °C for another 15 min without DMSO for drying.

The passivated films were prepared by letting the samples cool after the thermal annealing step and then using a 10 mM solution of PEA-I solution in dry 2-propanol (IPA). 100 µL of the passivation solution was put on the perovskite substrates and spin-coated for 20 s @ 3000 rpm. The samples were then dried by thermal annealing for 10 min @ 100 °C on the hot plate. In addition, the samples were put in a dry and dark atmosphere for at least 11 days; some were left in there for 36 days.

The samples for grain size effect investigation were prepared on Lumtec ITO-coated glass substrates. The ITO substrates were ultrasonicated for 30 min in detergent solution in deionized water, acetone, and isopropanol. After cleaning, the ITO substrates were treated with oxygen plasma for 7 min. The SnO_2 precursor was prepared by the reflux method,[88] which involved preparing a 0.1 M solution of tin(II) chloride dihydrate ($SnCl_2 \cdot H_2O$, Alfa Aesar) in a 1:19 butanol (Sigma-Aldrich)/deionized water mixture and heating it at 110 °C for 4 h. Then, the solution was spin-coated at 2000 rpm for 30 s and annealed at 130 °C for 60 min to obtain the SnO_2 layer. The perovskite precursor solution was prepared by dissolving 507.1 mg PbI_2, 73.4 mg $PbBr_2$ (Sigma-Aldrich), 22.4 mg methylammonium bromide (Sigma-Aldrich), and 172 mg formamidinium iodide (Greatcell Solar) in 1:4 DMSO:DMF. Then, 53 µL of 389.7 mg mL^{-1} cesium iodide (Sigma-Aldrich) in DMSO solution was added to the perovskite precursor solution. The perovskite precursor solution was then spin-coated at 1000 rpm for 10 s and then at 6000 rpm for 20 s. 250 µL of CB (anhydrous, Sigma-Aldrich) was dropped onto the sample roughly 5 s before the end of the program. After the coating, the films were annealed at 100 °C for 60 min on a hot plate.

The perovskite films with extremely large grains were obtained via a methylamine treatment.[85] The methylamine treatment was carried out with 230 mbar of methylamine partial pressure. The perovskite film was kept under this methylamine atmosphere for 10 s before the pressure was pumped up to 600 mbar, decreasing the methylamine partial pressure to ≈170 mbar during recrystallization.

Kelvin Probe Force Microscopy Measurements: KPFM was measured on an Oxford Instruments/Asylum Research MFP-3D Infinity AFM in a nitrogen glovebox (level of humidity below 0.3 %, level of oxygen below 0.1 %) for all experiments. The Pt/Ir-coated conductive cantilevers (Bruker Model: SCM-PIT-V2) had a typical resonance frequency of ≈75 kHz, a spring constant of 2 N m^{-1}, a tip radius of 25 nm, and a tip height of 10 to 15 µm. The topography feedback was performed with amplitude modulation (AM) on the first eigenmode, and the oscillation amplitude was kept to ≈20–30 nm for all measurements. A Zurich Instruments HF2 Lock-In amplifier was used for all heterodyne KPFM experiments,[68,69] to perform the KPFM feedback. The electric drive amplitude of the ω_E signal varied between 2 and 5 V depending on the obtained signal from the sample. The sample was grounded via the sample holder with an external wire to the ground level of the Zürich Lock-In Amplifier. The compensating V_{DC} was applied to the tip, minimizing the electrostatic tip–sample interactions. For SPV measurements, the sample was illuminated from below by a pulsed laser (Cobolt 06-01 Series) at 488 nm. The laser power was controlled by a custom-written code within the MFP3D's control software by the AFM controller (Asylum Research ARC2), which provided analog voltage to activate the illumination.

Optical Measurements: PL and tr-PL measurements were performed on a PicoQuant FluoTime300 fluorescence spectrometer with an excitation wavelength of 405 nm. The repetition rate was set as 40 and 1 MHz for steady-state and time-resolved measurements, respectively. A 455 nm longpass filter was placed between the sample and the detector to block the stray laser light.

UV–vis absorbance spectroscopy was carried out with a CARY 5000 UV-Vis spectrometer by Agilent Technologies.

X-ray Diffraction Measurements: The XRD measurements were performed on a Bruker D8 X-ray diffractometer with a Cu anode using the K(alpha) emission line between 5° and 70°. The measurements were made with a step resolution of 0.02° and a 192 s integration time per step.

Supporting Information

Supporting Information is available from the Wiley Online Library or from the author.

Acknowledgements

Y.Y. and P.N.R. contributed equally to this work. Y.Y. and S.A.L.W. acknowledge the SPP2196 project (Deutsche Forschungsgemeinschaft) for funding. The authors also thank Stefan Glunz (ISE Freiburg) for the discussions that inspired the implementation of the nano-IFM method.

Open access funding enabled and organized by Projekt DEAL.

Conflict of Interest

The authors declare no conflict of interest.

Data Availability Statement

The data that support the findings of this study are available from the corresponding author upon reasonable request.

Keywords

atomic force microscopy, charge carrier dynamics, Ideality factor, Kelvin probe force microscopy, perovskites, surface photovoltage spectroscopy

Received: June 5, 2023
Revised: July 31, 2023
Published online: October 18, 2023

[1] L. Protesescu, S. Yakunin, M. I. Bodnarchuk, F. Krieg, R. Caputo, C. H. Hendon, R. X. Yang, A. Walsh, M. V. Kovalenko, *Nano Lett.* **2015**, *15*, 3692.
[2] C. C. Stoumpos, C. D. Malliakas, M. G. Kanatzidis, *Inorg. Chem.* **2013**, *52*, 9019.
[3] T. J. Jacobsson, J.-P. Correa-Baena, M. Pazoki, M. Saliba, K. Schenk, M. Grätzel, A. Hagfeldt, *Energy Environ. Sci.* **2016**, *9*, 1706.
[4] K. X. Steirer, P. Schulz, G. Teeter, V. Stevanovic, M. Yang, K. Zhu, J. J. Berry, *ACS Energy Lett.* **2016**, *1*, 360.
[5] M. B. Johnston, L. M. Herz, *Acc. Chem. Res.* **2016**, *49*, 146.
[6] S. D. Stranks, G. E. Eperon, G. Grancini, C. Menelaou, M. J. Alcocer, T. Leijtens, L. M. Herz, A. Petrozza, H. J. Snaith, *Science* **2013**, *342*, 341.
[7] D. Shi, V. Adinolfi, R. Comin, M. Yuan, E. Alarousu, A. Buin, Y. Chen, S. Hoogland, A. Rothenberger, K. Katsiev, Y. Losovyj, X. Zhang, P. A. Dowben, O. F. Mohammed, E. H. Sargent, O. M. Bakr, *Science* **2015**, *347*, 519.
[8] R. E. Brandt, J. R. Poindexter, P. Gorai, R. C. Kurchin, R. L. Hoye, L. Nienhaus, M. W. Wilson, J. A. Polizzotti, R. Sereika, R. Zaltauskas, L. C. Lee, J. L. MacManus-Driscoll, M. Bawendi, V. Stevanovic, T. Buonassisi, *Chem. Mater.* **2017**, *29*, 4667.
[9] Y. Lei, Y. Xu, M. Wang, G. Zhu, Z. Jin, *Small* **2021**, *17*, 2005495.
[10] C. Aranda, A. Guerrero, J. Bisquert, *ACS Energy Lett.* **2019**, *4*, 741.
[11] D. Yang, X. Zhang, K. Wang, C. Wu, R. Yang, Y. Hou, Y. Jiang, S. Liu, S. Priya, *Nano Lett.* **2019**, *19*, 3313.
[12] M. Abdi-Jalebi, M. Ibrahim Dar, S. P. Senanayak, A. Sadhanala, Z. Andaji-Garmaroudi, L. M. Pazos-Outón, J. M. Richter, A. J. Pearson, H. Sirringhaus, M. Grätzel, R. H. Friend, *Sci. Adv.* **2019**, *5*, eaav2012.
[13] E. Halvani Anaraki, A. Kermanpur, M. T. Mayer, L. Steier, T. Ahmed, S.-H. Turren-Cruz, J. Seo, J. Luo, S. M. Zakeeruddin, W. R. Tress, T. Edvinsson, M. Grätzel, A. Hagfeldt, J.-P. Correa-Baena, *ACS Energy Lett.* **2018**, *3*, 773.
[14] N. Arora, M. I. Dar, A. Hinderhofer, N. Pellet, F. Schreiber, S. M. Zakeeruddin, M. Grätzel, *Science* **2017**, *358*, 768.
[15] S. Gharibzadeh, P. Fassl, I. M. Hossain, P. N. Rohrbeck, M. Frericks, M. Schmidt, T. Duong, M. R. Khan, T. Abzieher, B. A. Nejand, F. Schackmar, O. Almora, T. Feeney, R. Singh, D. Fuchs, U. Lemmer, J. P. Hofmann, S. A. L. Weber, U. W. Paetzold, *Energy Environ. Sci.* **2021**, *14*, 5875.
[16] C. Ma, N.-G. Park, *ACS Energy Lett.* **2020**, *5*, 3268.
[17] M. Stolterfoht, V. M. Le Corre, M. Feuerstein, P. Caprioglio, L. J. A. Koster, D. Neher, *ACS Energy Lett.* **2019**, *4*, 2887.
[18] E. Serpetzoglou, I. Konidakis, G. Kakavelakis, T. Maksudov, E. Kymakis, E. Stratakis, *ACS Appl. Mater. Interfaces* **2017**, *9*, 43910.
[19] H. Hempel, T. J. Savenjie, M. Stolterfoht, J. Neu, M. Failla, V. C. Paingad, P. Kužel, E. J. Heilweil, J. A. Spies, M. Schleuning, J. Zhao, D. Friedrich, K. Schwarzburg, L. D. A. Siebbeles, P. Dörflinger, V. Dyakonov, R. Katoh, M. J. Hong, J. G. Labram, M. Monti, E. Butler-Caddle, J. Lloyd-Hughes, M. M. Taheri, J. B. Baxter, T. J. Magnanelli, S. Luo, J. M. Cardon, S. Ardo, T. Unold, *Adv. Energy Mater.* **2022**, *12*, 2102776.
[20] E. Von Hauff, D. Klotz, *J. Mater. Chem. C* **2022**, *10*, 742.
[21] Y.-C. Chin, M. Daboczi, C. Henderson, J. Luke, J.-S. Kim, *ACS Energy Lett.* **2022**, *7*, 560.
[22] N. Li, A. Feng, X. Guo, J. Wu, S. Xie, Q. Lin, X. Jiang, Y. Liu, Z. Chen, X. Tao, *Adv. Energy Mater.* **2022**, *12*, 2103241.
[23] S. Zouhair, S.-M. Yoo, D. Bogachuk, J. P. Herterich, J. Lim, H. Kanda, B. Son, H. J. Yun, U. Würfel, A. Chahboun, M. K. Nazeeruddin, A. Hinsch, L. Wagner, H. Kim, *Adv. Energy Mater.* **2022**, *12*, 2200837.
[24] Y. Zhang, Y. Zhu, M. Hu, N. Pai, T. Qin, Y.-B. Cheng, U. Bach, A. N. Simonov, J. Lu, *J. Phys. Chem. Lett.* **2022**, *13*, 2792.
[25] G. Irde, S. M. Pietralunga, V. Sala, M. Zani, J. M. Ball, A. J. Barker, A. Petrozza, G. Lanzani, A. Tagliaferri, *Micron* **2019**, *121*, 53.
[26] S. M. Pietralunga, G. Irde, A. J. Barker, J. M. Ball, A. Petrozza, V. Sala, M. Zani, G. Lanzani, A. Tagliaferri, *Adv. Mater. Interfaces* **2020**, *7*, 2000297.
[27] S. K. Yadavalli, M. Chen, M. Hu, Z. Dai, Y. Zhou, N. P. Padture, *Scr. Mater.* **2020**, *187*, 88.
[28] D. Zhang, Y. Zhu, L. Liu, X. Ying, C.-E. Hsiung, R. Sougrat, K. Li, Y. Han, *Science* **2018**, *359*, 675.
[29] R. Egerton, P. Li, M. Malac, *Micron* **2004**, *35*, 399.
[30] J. Ran, O. Dyck, X. Wang, B. Yang, D. B. Geohegan, K. Xiao, *Adv. Energy Mater.* **2020**, *10*, 1903191.
[31] I. M. Hermes, S. A. Bretschneider, V. W. Bergmann, D. Li, A. Klasen, J. Mars, W. Tremel, F. Laquai, H.-J. Butt, M. Mezger, R. Berger, B. J. Rodriguez, S. A. L. Weber, *J. Phys. Chem. C* **2016**, *120*, 5724.
[32] I. M. Hermes, A. Best, L. Winkelmann, J. Mars, S. M. Vorpahl, M. Mezger, L. Collins, H.-J. Butt, D. S. Ginger, K. Koynov, S. A. L. Weber, *Energy Environ. Sci.* **2020**, *13*, 4168.
[33] Y. Yalcinkaya, I. M. Hermes, T. Seewald, K. Amann-Winkel, L. Veith, L. Schmidt-Mende, S. A. Weber, *Adv. Energy Mater.* **2022**, 2202442.
[34] Y. Shao, Y. Fang, T. Li, Q. Wang, Q. Dong, Y. Deng, Y. Yuan, H. Wei, M. Wang, A. Gruverman, J. Shielda, J. Huang, *Energy Environ. Sci.* **2016**, *9*, 1752.

[35] B. Conings, J. Drijkoningen, N. Gauquelin, A. Babayigit, J. D'Haen, L. D'Olieslaeger, A. Ethirajan, J. Verbeeck, J. Manca, E. Mosconi, F. De Angelis, H.-G. Boyen, *Adv. Energy Mater.* **2015**, *5*, 1500477.
[36] V. W. Bergmann, S. A. Weber, F. Javier Ramos, M. K. Nazeeruddin, M. Grätzel, D. Li, A. L. Domanski, I. Lieberwirth, S. Ahmad, R. Berger, *Nat. Commun.* **2014**, *5*, 5001.
[37] I. M. Hermes, Y. Hou, V. W. Bergmann, C. J. Brabec, S. A. Weber, *J. Phys. Chem. Lett.* **2018**, *9*, 6249.
[38] S. A. Weber, I. M. Hermes, S.-H. Turren-Cruz, C. Gort, V. W. Bergmann, L. Gilson, A. Hagfeldt, M. Graetzel, W. Tress, R. Berger, *Energy Environ. Sci.* **2018**, *11*, 2404.
[39] E. M. Lanzoni, T. Gallet, C. Spindler, O. Ramirez, C. K. Boumenou, S. Siebentritt, A. Redinger, *Nano Energy* **2021**, *88*, 106270.
[40] E. Strelcov, S. Jesse, Y.-L. Huang, Y.-C. Teng, I. I. Kravchenko, Y.-H. Chu, S. V. Kalinin, *ACS Nano* **2013**, *7*, 6806.
[41] L. Collins, A. Belianinov, S. Somnath, N. Balke, S. V. Kalinin, S. Jesse, *Sci. Rep.* **2016**, *6*, 30557.
[42] L. Collins, M. Ahmadi, J. Qin, Y. Liu, O. S. Ovchinnikova, B. Hu, S. Jesse, S. V. Kalinin, *Nanotechnology* **2018**, *29*, 44.
[43] Z. Schumacher, A. Spielhofer, Y. Miyahara, P. Grutter, *Appl. Phys. Lett.* **2017**, *110*, 5.
[44] B. Grévin, O. Bardagot, R. Demadrille, *Beilstein J. Nanotechnol.* **2020**, *11*, 323.
[45] V. Aubriet, K. Courouble, O. Bardagot, R. Demadrille, Ł. Borowik, B. Grévin, *Nanotechnology* **2022**, *33*, 225401.
[46] J. Murawski, T. Graupner, P. Milde, R. Raupach, U. Zerweck-Trogisch, L. Eng, *J. Appl. Phys.* **2015**, *118*, 15.
[47] E. Johnson, *Phys. Rev.* **1958**, *111*, 153.
[48] D. Cavalcoli, A. Cavallini, *Phys. Status Solidi c* **2010**, *7*, 1293.
[49] J. T.-W. Wang, Z. Wang, S. Pathak, W. Zhang, D. W. deQuilettes, F. Wisnivesky-Rocca-Rivarola, J. Huang, P. K. Nayak, J. B. Patel, H. A. M. Yusof, Y. Vaynzof, R. Zhu, I. Ramirez, J. Zhang, C. Ducati, C. Grovenor, M. B. Johnston, D. S. Ginger, R. J. Nicholas, H. J. Snaith, *Energy Environ. Sci.* **2016**, *9*, 2892.
[50] G. Alkhalifah, A. D. Marshall, F. Rudayni, S. Wanigasekara, J. Z. Wu, W.-L. Chan, *J. Phys. Chem. Lett.* **2022**, *13*, 6711.
[51] S. Wood, D. O'Connor, C. W. Jones, J. D. Claverley, J. C. Blakesley, C. Giusca, F. A. Castro, *Sol. Energy Mater. Sol. Cells* **2017**, *161*, 89.
[52] L. Kronik, Y. Shapira, *Surf. Sci. Rep.* **1999**, *37*, 1.
[53] Q. Zhou, B. Wang, R. Meng, J. Zhou, S. Xie, X. Zhang, J. Wang, S. Yue, B. Qin, H. Zhou, Y. Zhang, *Adv. Funct. Mater.* **2020**, *30*, 2000550.
[54] I. Grill, M. F. Aygüler, T. Bein, P. Docampo, N. F. Hartmann, M. Handloser, A. Hartschuh, *ACS Appl. Mater. Interfaces* **2017**, *9*, 37655.
[55] T. Kirchartz, F. Deledalle, P. S. Tuladhar, J. R. Durrant, J. Nelson, *J. Phys. Chem. Lett.* **2013**, *4*, 2371.
[56] C. Van Berkel, M. Powell, A. Franklin, I. French, *J. Appl. Phys.* **1993**, *73*, 5264.
[57] D. Prochowicz, R. Runjhun, M. M. Tavakoli, P. Yadav, M. Saski, A. Q. Alanazi, D. J. Kubicki, Z. Kaszkur, S. M. Zakeeruddin, J. Lewiński, M. Grätzel, *Chem. Mater.* **2019**, *31*, 1620.
[58] P. Caprioglio, C. M. Wolff, O. J. Sandberg, A. Armin, B. Rech, S. Albrecht, D. Neher, M. Stolterfoht, *Adv. Energy Mater.* **2020**, *10*, 2000502.
[59] A. Dasgupta, S. Mahesh, P. Caprioglio, Y.-H. Lin, K.-A. Zaininger, R. D. Oliver, P. Holzhey, S. Zhou, M. M. McCarthy, J. A. Smith, M. Frenzel, M. G. Christoforo, J. M. Ball, B. Wenger, H. J. Snaith, *ACS Energy Lett.* **2022**, *7*, 2311.
[60] M. Nonnenmacher, M. o'Boyle, H. K. Wickramasinghe, *Appl. Phys. Lett.* **1991**, *58*, 2921.
[61] L. Kelvin, *Lond. Edinb. Dublin Philos. Mag. J. Sci.* **1898**, *46*, 82.
[62] J. Weaver, D. W. Abraham, *J. Vac. Sci. Technol. B Microelectron. Nanometer Struct. Process. Meas. Phenom.* **1991**, *9*, 1559.
[63] Y. Martin, D. W. Abraham, H. K. Wickramasinghe, *Appl. Phys. Lett.* **1988**, *52*, 1103.
[64] U. J. Bahnmüller, H. Kuper, T. Seewald, Y. Yalcinkaya, J. A. Becker, L. Schmidt-Mende, S. A. Weber, S. Polarz, *Nanomaterials* **2021**, *11*, 3057.
[65] W. Zhang, S. Pathak, N. Sakai, T. Stergiopoulos, P. K. Nayak, N. K. Noel, A. A. Haghighirad, V. M. Burlakov, D. W. DeQuilettes, A. Sadhanala, W. Li, L. Wang, D. S. Ginger, R. H. Friend, H. J. Snaith, *Nat. Commun.* **2015**, *6*, 10030.
[66] P. Rohrbeck, *Master thesis*, Johannes Gutenberg University Mainz, **2021**.
[67] D. Toth, B. Hailegnaw, F. Richheimer, F. A. Castro, F. Kienberger, M. C. Scharber, S. Wood, G. Gramse, *ACS Appl. Mater. Interfaces* **2020**, *12*, 48057.
[68] J. L. Garrett, J. N. Munday, *Nanotechnology* **2016**, *27*, 24.
[69] A. Axt, I. M. Hermes, V. W. Bergmann, N. Tausendpfund, S. A. L. Weber, *Beilstein J. Nanotechnol.* **2018**, *9*, 1809.
[70] Z. Xiao, Q. Dong, C. Bi, Y. Shao, Y. Yuan, J. Huang, *Adv. Mater.* **2014**, *26*, 6503.
[71] X. Yang, Y. Wei, F. Huang, S. Jin, D. Luo, Y. Fang, Y. Zhao, Q. Guo, Y. Huang, L. Fan, J. Wu, *Sol. Energy* **2019**, *177*, 299.
[72] J. Bing, S. Huang, A. W. Y. Ho-Baillie, *Energy Technol.* **2020**, *8*, 1901114.
[73] Y. Guo, S. Yuan, D. Zhu, M. Yu, H.-Y. Wang, J. Lin, Y. Wang, Y. Qin, J.-P. Zhang, X.-C. Ai, *Phys. Chem. Chem. Phys.* **2021**, *23*, 6162.
[74] E. Regalado-Pérez, E. B. Díaz-Cruz, J. Landa-Bautista, N. R. Mathews, X. Mathew, *ACS Appl. Mater. Interfaces* **2021**, *13*, 11833.
[75] S. Y. Leblebici, L. Leppert, Y. Li, S. E. Reyes-Lillo, S. Wickenburg, E. Wong, J. Lee, M. Melli, D. Ziegler, D. K. Angell, D. F. Ogletree, P. D. Ashby, F. M. Toma, J. B. Neaton, I. D. Sharp, A. Weber-Bargioni, *Nat. Energy* **2016**, *1*, 16093.
[76] D. Prochowicz, R. Runjhun, M. M. Tavakoli, P. Yadav, M. Saski, A. Q. Alanazi, D. J. Kubicki, Z. Kaszkur, S. M. Zakeeruddin, J. Lewiński, M. Grätzel, *Chem. Mater.* **2019**, *31*, 1620.
[77] V. W. Bergmann, S. A. L. Weber, F. Javier Ramos, M. K. Nazeeruddin, M. Grätzel, D. Li, A. L. Domanski, I. Lieberwirth, S. Ahmad, R. Berger, *Nat. Commun.* **2014**, *5*, 5001.
[78] V. W. Bergmann, Y. Guo, H. Tanaka, I. M. Hermes, D. Li, A. Klasen, S. A. Bretschneider, E. Nakamura, R. Berger, S. A. Weber, *ACS Appl. Mater. Interfaces* **2016**, *8*, 19402.
[79] G. D. Tainter, M. T. Hörantner, L. M. Pazos-Outón, R. D. Lamboll, H. Āboliņš, T. Leijtens, S. Mahesh, R. H. Friend, H. J. Snaith, H. J. Joyce, F. Deschler, *Joule* **2019**, *3*, 1301.
[80] R. Ciesielski, F. Schäfer, N. F. Hartmann, N. Giesbrecht, T. Bein, P. Docampo, A. Hartschuh, *ACS Appl. Mater. Interfaces* **2018**, *10*, 7974.
[81] D. W. DeQuilettes, S. Jariwala, S. Burke, M. E. Ziffer, J. T.-W. Wang, H. J. Snaith, D. S. Ginger, *ACS Nano* **2017**, *11*, 11488.
[82] Y. Shao, Y. Fang, T. Li, Q. Wang, Q. Dong, Y. Deng, Y. Yuan, H. Wei, M. Wang, A. Gruverman, J. Shield, J. Huang, *Energy Environ. Sci.* **2016**, *9*, 1752.
[83] K. Fu, C. T. Nelson, M. C. Scott, A. Minor, N. Mathews, L. H. Wong, *Nanoscale* **2016**, *8*, 4181.
[84] J. Herterich, M. Unmüssig, L. Wagner, G. Loukeris, J. Faisst, M. List, M. Kohlstädt, U. Würfel, *Energy Technol.* **2022**, *10*, 2100868.
[85] E. R. Schütz, A. Fakharuddin, Y. Yalcinkaya, E. Ochoa-Martinez, S. Bijani, A. R. b. Mohd Yusoff, M. Vasilopoulou, T. Seewald, U. Steiner, S. A. Weber, L. Schmidt-Mende, *APL Mater.* **2022**, *10*, 081110.
[86] S. Wheeler, F. Deledalle, N. Tokmoldin, T. Kirchartz, J. Nelson, J. R. Durrant, *Phys. Rev. Appl.* **2015**, *4*, 024020.
[87] N. Courtier, *Phys. Rev. Appl.* **2020**, *14*, 024031.
[88] C. Chen, Y. Jiang, J. Guo, X. Wu, W. Zhang, S. Wu, X. Gao, X. Hu, Q. Wang, G. Zhou, Y. Chen, J.-M. Liu, K. Kempa, J. Gao, *Adv. Funct. Mater.* **2019**, *29*, 1900557.